Understanding Residual Stress in Direct Energy Deposition: A Comprehensive Study of GRCop-42 using Finite Element Simulation and Energy Dispersive X-ray Diffraction

A Thesis

Presented to the Faculty of the Graduate School

of Cornell University

In Partial Fulfillment of the Requirements for the Degree of

Master of Science

by

Yuhui Li

August 2023

ABSTRACT

The development of residual stress in metal material additive manufacturing brings a significant obstacle to achieving parts with good quality. The residual stress can be destructive as the structural integrity and mechanical properties are seriously influenced during the manufacturing process. In this work, a finite element method based thermomechanical model is created to simulate the process of direct energy deposition for a copper alloy, GRCop-42. The thermal history of the deposition process is captured, and the development of residual stress & strain is calculated. The result of residual strain development inside the part is compared with the experimental measurement by energy dispersive x-ray diffraction. From the comparison, the result from thermomechanical model shows a high level of consistency with the EDD measurement result in the middle section of the part. However, the EDD result shows a higher residual strain at the left end of the specimen. Non-uniform geometry of printed specimen due to the bulging corners is measured and proved to be the reason for the discrepancy between simulation result and experimental result. Different laser parameters and material properties were also tested in the thermomechanical model to study their influence on the residual stress in additive manufacturing process. The work of this paper provides an approach to understand the development of residual stress, which will be crucial in enhancing the performance of metal additive manufacturing in a wide range of industrial applications.

BIOGRAPHICAL SKETCH

Yuhui Li pursued his Bachelor of Science in Mechanical Engineering from University of California, San Diego. His research focused on finite element analysis, 3D modeling and additive manufacturing. He joined Cornell University in Summer 2021 to pursue his Master of Science in Mechanical Engineering. At Cornell University, he joined the Laboratory of Advanced Materials and Manufacturing and worked under the guidance of Prof. Atieh Moridi. His MS research project included the thermomechanical simulation of direct energy deposition and energy dispersive x-ray diffraction analysis on residual strain.

ACKNOWLEDGMENTS

I would like to thank my committee members for their guidance on my research project. I would like to express my heartfelt thankfulness to Prof. Atieh Moridi for offering me the opportunity to work in her group and to complete this work to the best of my abilities. I could not have undertaken this journey without her guidance and support. I am also grateful to my lab colleagues, especially Adrita Dass and Ashlee Gabourel, for their help on my research. I appreciate the people at Cornell High Energy Synchrotron Source and Cornell Center for Materials Research for their assistance in my experiments. I would also like to thank my family and my friends for their love and support. Without their encouragement and motivation, it would be impossible for me to overcome the obstacles in the past two years.

TABLE OF CONTENTS

LIST OF FIGURES

LIST OF TABLES

CHAPTER ONE

INTRODUCTION AND BACKGROUND

1.1 Overview

Metal material additive manufacturing (AM), also known as metal 3D printing, has emerged as a revolutionary technology with significant potential in many industries. Metal AM enables the production of complex geometries and unique material properties that would be impracticable or challenging for traditional manufacturing methods [1]. Because of the elimination of complex tooling and material waste, additive manufacturing allows for expedited prototyping and production, which holds particular significance in time-sensitive industries such as medical and aerospace, where the efficiency is of utmost importance [2]. At the same time, additive manufacturing enables the production of parts with different lattice structures and gradients, which improves the mechanical properties, such as yield strength and fatigue life [3]. Overall, metal additive manufacturing brings a revolution to the traditional manufacturing processes through its exceptional benefits, such as design flexibility, manufacturing speed and production quality.

1.1.1 Direct Energy Deposition (DED)

Some common types of metal additive manufacturing are powder bed fusion, electron beam melting, selective laser melting and directed energy deposition, among which the direct energy deposition has certain advantages that make it a popular choice for industry. The manufacturing process of metal AM involves material deposition and melting by high energy source, like a laser beam [4]. Different from other AM methods, in DED, the material deposition and laser beam

heating happens simultaneously, which significantly increases the production efficiency. In DED, the powder or wire material feedstock is introduced into the molten pool created by the energy source, and the material is deposited layer by layer to build up the part [5]. The material choice of DED can be diverse, including ceramics, composites and metals, and such capability supports the multiple alloy printing [6,7].

1.1.2 GRCop-42

The material used for direct energy deposition in this work is GRCop-42. GRCop-42 is a copper-chromium-niobium alloy developed by NASA for space missions. Designed with the purpose for additive manufacturing, GRCop-42 has a great thermal conductivity and thermal cycling stability. The excellent mechanical strength and corrosion resistance make it a perfect choice for the space shuttle components, such as propulsion components [8].

1.2 Nature of Residual Stress

In the AM, several characteristics describe the thermal behavior during the deposition: fast heating with a steep temperature gradient, rapid solidification, repetitive melting and remelting [9-12]. The combined influence of these factors leads to the development of residual stress. The existence of residual stress can significantly expedite the degradation of materials in terms of fatigue life, stress corrosion resistance and fracture toughness [13-15]. Therefore, controlling the residual stress in AM is crucial for the manufacturers to improve the structural integrity and mechanical performance of the components [16]. Because the complex stress state caused by the recurring heating and cooling evolves quickly and randomly during the AM process, the precise prediction of the residual stress development is challenging to be achieved [17]. In order to reveal the mechanism of residual stress development, significant research endeavors have been

made by researchers in past years [18-31], both in experimental methods and numerical simulations.

1.3 Residual Stress Development: Experimental Measurement and Simulation

1.3.1 Destructive Measurement

The categorization of experimental measurement techniques for residual stress can be broadly divided into two groups: destructive and non-destructive approaches [18]. In the category of destructive measurement, deep-hole drilling method is commonly used. In this method, the diameter change in a reference hole is recorded before and after stress releasing process to calculate the bi-axial residual stresses, as reported by R.H. Leggatt et al [19]. A multiple-cut contour method, proposed by F. Hosseinzadeh et al, is used to generate a 2D map of residual stress distribution in a thin-walled welded pipe. The residual stress distribution is proved to be governed by through-wall bending and deformation [20].

1.3.2 Non-destructive Measurement

The non-destructive methods provide an approach to measure the residual stress without damaging the specimen. Therefore, an increasing number of non-destructive methods were proposed in the past few years. The diffraction method is one of the most popular approaches in the non-destructive measurements [18]. Neutron diffraction, x-ray diffraction and x-ray synchrotron diffraction are three major types of diffraction techniques, and the x-ray synchrotron diffraction has the best performance than the others [17]. X-ray synchrotron diffraction outmatches the other techniques because it allows a smaller gauge volume and a shorter sampling time, and it enables the measurement at various depths under the surface of the sample.

Therefore, the x-ray synchrotron proves to be better suited for high-resolution residual stress calculation [21]. In x-ray synchrotron diffraction, the change of interplanar spacing in the material is captured and used in the Bragg's law to calculate the residual elastic strain, and residual stress is calculated from the strain by Hooke's law [22]. But one of the limitation of X-ray synchrotron residual stress measurement is that it requires multiple strain components, stiffness tensor and assumptions to calculate an accurate stress. The residual strain measurement of 4-point bended Ti64 alloy using x-ray synchrotron diffraction conducted by M. Croft et al shows the level of measurement precision to be 1.5×10^(-5) or higher [23]. The research conducted by M.L. Suominen et al. shows a successful measurement of both elastic and plastic strain in a Nicole sample using x-ray synchrotron diffraction [24].

1.3.3 Simulation of Residual Stress Development

Due to the numerous variables involved in metal AM, experimental measurements of residual stress are costly and time consuming [25]. Therefore, numerical analysis on the residual stress is performed by researchers, and an increasing number of simulations model of AM process have been created to calculate the residual stress. In order to make the simulation model closely match the real AM process, many techniques are invented, such as heat source model and progressive activation element [26,27]. To simulate the heat input in AM, a widely used heat source model in thermal simulation was first proposed by J. Goldak, and it described a 3D gaussian distributed heat generation with a double ellipsoid shape. Most of the simulation models consist of the thermal simulation for temperature field and the mechanical simulation for residual stress calculation [28]. The numerical simulation provides not only the residual stress but also thermal and mechanical data from the AM process. T. DebRoy et al created a thermomechanical model that integrates the heat transfer calculation, the material deposition simulation and the residual

stress calculation, and the residual stress result from their model shows a strong agreement with the experimentally measured data [29]. The influence of different manufacturing parameters on residual stress is investigated by G. Vastola [30] and O. Fergani [31].

1.4 Thesis Objectives

The objective for this thesis aims to provide both experimental and numerical analysis on the development of residual stress during additive manufacturing process. In this work, a 2-layer sample, a 5-layer sample and an 8-layer sample of GRCop-42 is manufactured by DED. The energy dispersive x-ray diffraction is performed on these samples to experimentally measure residual strain inside the samples. Based on the material properties of printed samples and the DED process setup, a thermomechanical simulation model is created on ABAQUS CAE to simulate the DED process of these samples and to calculate the thermal history and residual stress. The residual strain result from simulation model is compared with the EDD analysis result to validate the simulation model. Discrepancy between the results is explained. The influence of different process parameters and material properties on the residual stress is tested and discussed.

CHAPTER TWO

Residual Stress Measurement and Simulation

2.1 Thermomechanical Modeling

The thermomechanical model simulating the DED process of GRCop-42 is created within ABAQUS CAE. ABAQUS CAE is a software application that supports finite element analysis of mechanical components and visualizing the FEA results. To calculate the residual stress development, the thermomechanical model starts with the thermal analysis that calculates the transient temperature of DED process. The Goldak heat soured model, which describes a 3D gaussian distributed volumetric heat flux, is implemented by the DFLUX user subroutine code to simulate energy input by the laser beam during the material depositing process. The heat source model cooperates with the layer-by-layer material deposition process model, which is realized by the element birth technique using Python code. In this geometry change process, the rate of element birth in a single layer matches the scanning rate of the laser beam, and then the ongoing layer is activated while the preceding layers are deactivated. The Selective Mesh Coarsening (SMC) method is employed to improve efficiency. The result of temperature history from thermal analysis is imported to the mechanical analysis to calculate the residual stress and strain. The outcomes from the thermomechanical model are the thermal history, residual stress and residual strain of the part during the DED process.

2.1.1 Assumptions

To accurately calculate the residual stress result, some assumptions are made align with the AM Process. The deposited layers are considered to have a perfectly flat surface. The densities of the materials are assumed to be constant. The material and heat loss due to

vaporization is ignored. The air flow in the environment is considered to be static. The effects of strains induced by solid-state phase transformation are also ignored [29].

2.1.2 Heat source model and boundary conditions

In order to simulate the laser beam heat input, a heat source model is required. The Goldak Heat Source Model is the most common heat source model which describes the 3D Gaussian distributed body heat flux from the laser beam. The heat flux is described in Eq. (1).

$$q(x,y,z) = \begin{cases} \frac{6\sqrt{3}Qf_{fr}}{\pi\sqrt{\pi}abc_{fr}} \exp\left\{-3\left[\frac{z^2}{b^2}+\frac{y^2}{a^2}+\frac{x^2}{c_r^2}\right]\right\}, (x \le 0) \\ \frac{6\sqrt{3}Qf_{fr}}{\pi\sqrt{\pi}abc_{fr}} \exp\left\{-3\left[\frac{z^2}{b^2}+\frac{y^2}{a^2}+\frac{x^2}{c_f^2}\right]\right\}, (x \ge 0) \end{cases} \quad (1)$$

Here qx,y,z is the volumetric power density; a, b and cfr are the length of semi axis of the ellipsoid in the volumetric heat source model shown in the Fig. 1. The area constrained by the red-line boundary is where the heat flux is calculated and is used as the laser heat input for the simulation. x, y and z are the distance to the laser spot center, which is the origin of the coordinate system. The f_f and f_r are the distribution factors of the heat deposited in the front and rear ellipsoids [28]. A conditional requirement for ff and fr is stated in Eq. (2):

$$f_f + f_r = 2 \quad (2)$$

Q is the heat input from the heat source per unit time. In this thermomechanical model, the Q is affected by the laser power and the laser absorptivity of metal powder. The calculation of Q is described in Eq. (3), where P is power of laser and η is the laser absorptivity of material.

$$Q = P\eta \quad (3)$$

The value of ellipsoids semi axes a,b,c is initially set according to the size of material deposited in each step of element birth. The semi-axes of the ellipsoid a, b, c in the directions x, y, z are adjusted such that the power density falls to 5% of q at the surface of the ellipsoid [27]. With the proper value defined for a, b, c, the deposited material in the simulation can reach the melting temperature of GRCop-42. Using these equations, the Goldak model can be encoded into the DFLUX user subroutine code. The DFLUX is one of the user subroutine code in ABAQUS that describes the thermal loading. It defines a nonuniform distributed heat flux as a function of position, time, temperature, element number, integration point number in a heat transfer analysis.

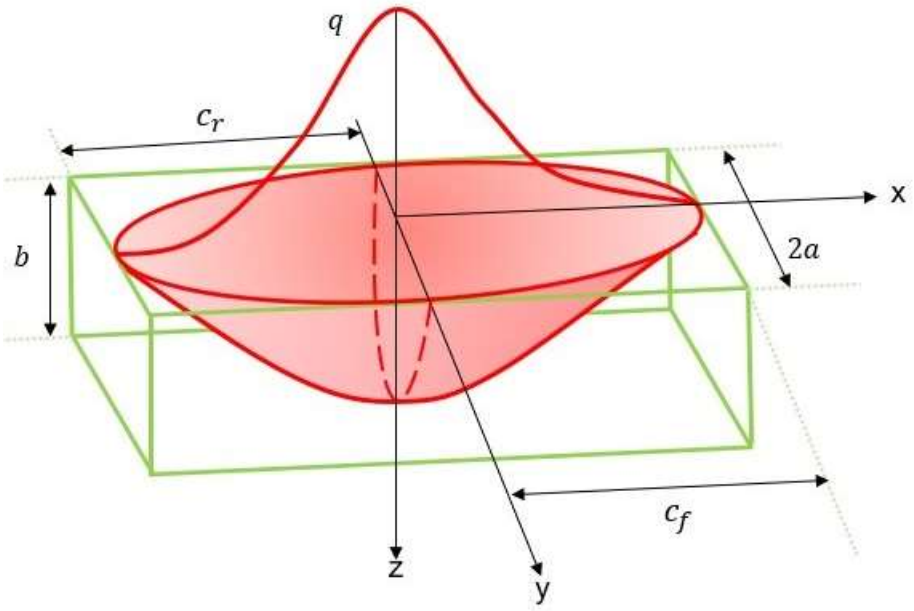

Fig. 1. *Goldak heat source model, a double ellipsoid heat source model*

The initial condition is set as described in Eq. (4). The initial temperature is set to be the room temperature. And the boundary condition of the heat source model is set as described in Eq. (5):

$$T(x, y, z, 0) = T_0 \tag{4}$$

$$k\frac{\partial T}{\partial n} - q + h(T - T_0) + \sigma_b \varepsilon_b (T^4 - T_0^4) = 0,\ (x, y, z) \in S_n \quad (5)$$

Here T_0 is the room temperature, which is set to be 25 Celsius degrees. n is the size of a normal vector on the model surface; h is the convection heat transfer coefficient between the metal material and the surrounding environment, which is air in this model; σ_b is Stefan-Boltzmann constant; ε_b is the emissivity of the metal material; S_n is the model surface [27].

With the heat input model defined by equations above, the thermal field can be obtained. The next step is to obtain the stress field by first calculating the residual strain inside the part. The total strain increment consists of different strain increments, as shown in the Eq. (6):

$$\Delta\varepsilon_{total} = \Delta\varepsilon_{elastic} + \Delta\varepsilon_{plastic} + \Delta\varepsilon_{therm} \quad + \Delta\varepsilon_V \quad (6)$$

$$\Delta\varepsilon_{elastic} = D^{-1}\sigma_{elastic} \quad (7)$$

$$\Delta\varepsilon_{thermal} = \alpha(T)\Delta T \quad (8)$$

Here $\Delta\varepsilon_{elastic}$ is elastic strain increment; $\Delta\varepsilon_{plastic}$ is plastic strain increment; $\Delta\varepsilon_{thermal}$ is thermal strain increment, and $\Delta\varepsilon_V$ is strain increment induced by solid-state phase transformation, which is assumed to be zero. D is the elastic stiffness matrix. $\sigma_{elastic}$ is the stress increment due to the elastic strain increment. α is the thermal expansion coefficient of metal material and it is a temperature dependent parameter.

2.1.3 Material properties, geometry and process parameters

The material used to manufacture specimens in this work is GRCop-42. GRCop-42 is a copper alloy with 4% chromium and 2% niobium that NASA developed for use in rocket propulsion components. It has high thermal conductivity, excellent creep resistance, low-cycle

fatigue life, and strength at elevated temperatures [32]. GRCop-42 is designed to have better laser absorptivity such that it could be applied in AM to manufacture complex and intricate designs, such as combustion chamber liners and fuel injector face plates. In this work, the mechanical and thermal properties of GRCop-42 are collected from multiple sources in literature [33-36]. The thermal expansion coefficient and density of GRCop-42 are temperature dependent properties, shown in Table 2. However, because GRCop-42 is a newly developed and classified material in the past several years, the laser absorption coefficient data is difficult to be found in the literature. Here, an estimated laser absorption coefficient of 7.5% is proposed in the simulation model based on the value of pure copper, which is less than 5%.

Table. 1. *Mechanical and thermal properties of GrCop-42*

Material	**GrCop-42**
Conductivity	344 Wm-1K-1
Specific Heat	385 Jkg−1·K−1
Young's Modulus	130 GPa
Poisson's Ratio	0.34
Yield Stress	210 MPa
Laser Absorption Coefficient	7.5%

Table. 2. *Temperature dependent properties of GrCop-42*

Thermal Expansion Coefficient	**Temperature**	**Density**	**Temperature**
1.64e-5	100C	8900 kg/m3	25C
1.85e-5	250C	7940 kg/m3	1083C
2.02e-5	500C	7924 kg/m3	1100C
2.48e-5	925C	7846 kg/m3	1200C

In this work, three samples with different number of layers are manufactured by direct energy deposition (DED), as shown in the Fig. 2. DED is a type of metal AM processes. It adds material along with the heat input simultaneously. A typical DED machine consists of a nozzle that shoots the laser beam and feeds metal powder. A 2-layer sample, a 5-layer sample and an 8-layer sample are manufactured. By direct measurement from the manufactured sample, the dimensions in X, Y and Z direction of each sample are collected. Shown in the Table 3, the X and Y dimension for these samples are almost the same, but the average layer height of 2 layers sample is a little bit thicker than the other samples. For each sample, the materials are deposited on a large stainless-steel substrate. All these data are used to create the geometry of different samples for thermomechanical simulation model.

Table. 3. *Dimension of samples in simulation*

2 Layer Sample	**5 Layer Sample**	**8 Layer Sample**	**SS Substrate**
X: 16 mm	X: 16 mm	X: 16 mm	X: 24 mm
Y: 1.6 mm	Y: 1.7 mm	Y: 1.77 mm	Y: 5 mm
Z: 0.64 mm	Z: 1.24 mm	Z: 1.9 mm	Z: 5 mm
Average Layer Height: 0.32 mm	Average Layer Height: 0.248 mm	Average Layer Height: 0.238mm	

The laser parameters are initially set with a power of 1500W, a scanning speed of 1200mm/min and a beam radius of 1.1mm. With these parameters, the temperature inside the melt pool in simulation is slightly above the melting point of GRCop-42, which is 1080 Celsius degree.

After creating and validating the thermomechanical model with the initial laser parameters, different laser parameters and material properties are tested in order to study their

influence on the residual stress development. In this work, only one parameter is changed at one time so that the influence of that single process parameter can be clearly observed. The laser parameters and material properties tested in this work are shown in Table 4.

Table. 4. *Different process parameters and different material properties for test*

Laser power	1200 W	1500 W	1800 W	2000 W
Scanning Speed	800 mm/min	960 mm/min	1200 mm/min	2400 mm/min
Yield Stress	186 MPa		880 MPa	
Thermal Expansion Coefficient	1.87e-05		2.48e-05	
Laser Absorptivity	7.5%		40%	

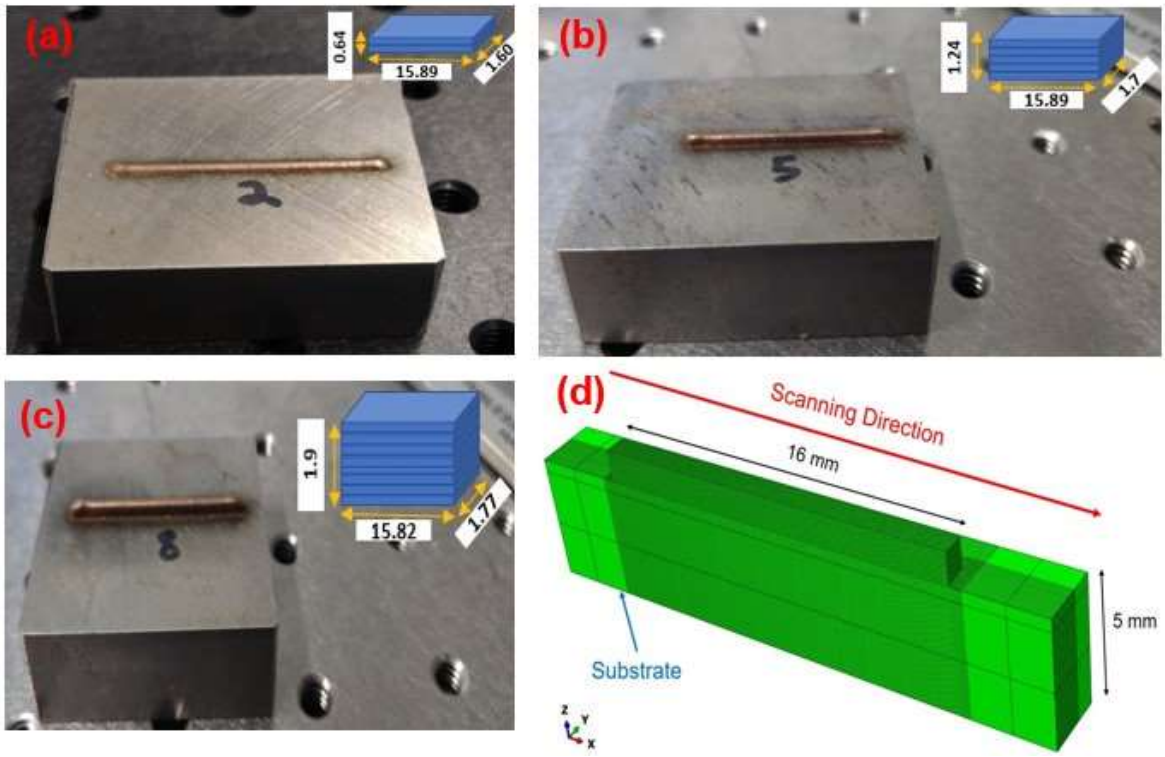

Fig. 2. *DED manufactured GRCop-42 samples (a) a 2-layer sample (b) a 5-layer sample (c) an 8-layer sample and (d) center-cut view of the geometry for thermomechanical analysis*

2.1.4 Geometry mesh selection and modeling of material deposition

The geometry of the model consists of the layers of deposited layers and the substrate. The center-cut view of the 8 layer geometry is shown in Fig. 2. In the thermal model that generates the temperature history results, an 8-node brick like linear heat transfer mesh named DC3D8 is applied. Another 3D stress type mesh called C3D8R is used in the mechanical model to calculate residual stress. C3D8R is an 8-node linear brick that has reduced integration and hourglass control. In order to achieve the maximum computational efficiency and the highest accuracy of result, selective mesh control is applied. Multiple mesh sizes for the deposited layer area are tested. The convergence of residual stress results with different mesh size is examined and the computation time for each simulation is recorded. It is found that the mesh size of 0.16 mm in the deposited layers and 1.5 mm in the substrate gives a convergent residual stress result with a moderate computational cost. The average time cost to finish the simulation for an 8-layer sample is 6.5 hours. The total element numbers of the mesh for each sample are listed in the Table 5.

Table. 5. Element size and total number of elements for different samples

Element Size		**Number of Elements**		
Deposited Layers	**Substrate**	**2 Layer**	**5 Layer**	**8 Layer**
0.16 mm	1.5 mm	21360	38640	55920

The nature of DED process requires the material deposition and heat input to happen simultaneously. Therefore, model change is required when the deposition is ongoing layer by layer. The element birth technique is recognized to be the best and most commonly used method in ABAQUS to realize the model change in simulation. The word birth means activation of elements, and the idea of model change in this model is to activate the elements at the place

where the laser heat source passes. A python code was created to describe the status of each element in every step and to control the activation of elements.

The number of elements of each step is defined by the laser process parameters and the sample geometry. In this work, the laser speed is 1200mm/min, and it only travels from left to right end once per layer. The length of deposited layers is 16mm. Based on the calculation, the material deposition head of DED system needs 0.8 seconds to travel the whole track of a single layer. There are 10 steps for each deposited layer, and the time for each step is set to 0.08 seconds to coordinate with the laser scanning speed. Twenty fixed time increments are set for each step to reduce the computational cost. The geometry change begins with an activated substrate and deactivated deposited layers. With the laser heat source activated, the elements of newly deposited material starts to be generated step by step. In the example of the 8-layer sample, 576 elements in a 1.6mm x 1.6mm x 0.2mm volume are activated in each step. After 10 steps, the deposition of material in one layer is completed.

2.1.5 Data collection

The manufacturing process of samples in this work includes the heating process for material deposition and the cooling process after the deposition finished. The average time for the sample cooling to the room temperature is one hour. Different strategies are applied for the data collection. Most of the data is collected both during the deposition and after the cooling process. The temperature history result is collected along the center line in x direction of a deposited layer right after the deposition of that layer is finished. The temperature data on the center point of first layer is also collected to monitor the thermal cycle all over the simulation. For the residual stress and strain result, the data is collected in each layer after the whole sample

cools down to the room temperature. In an effort to get the most accurate result of residual stress, 7 evenly spaced lines parallel to the x axis are set through the y direction, then the data on each line is acquired and averaged to give a region of residual stress development. The data on the lines with an angle between -2 degree to 2 degree from center line in x direction is also collected in order to be compared with the EDD results with different diffraction angle.

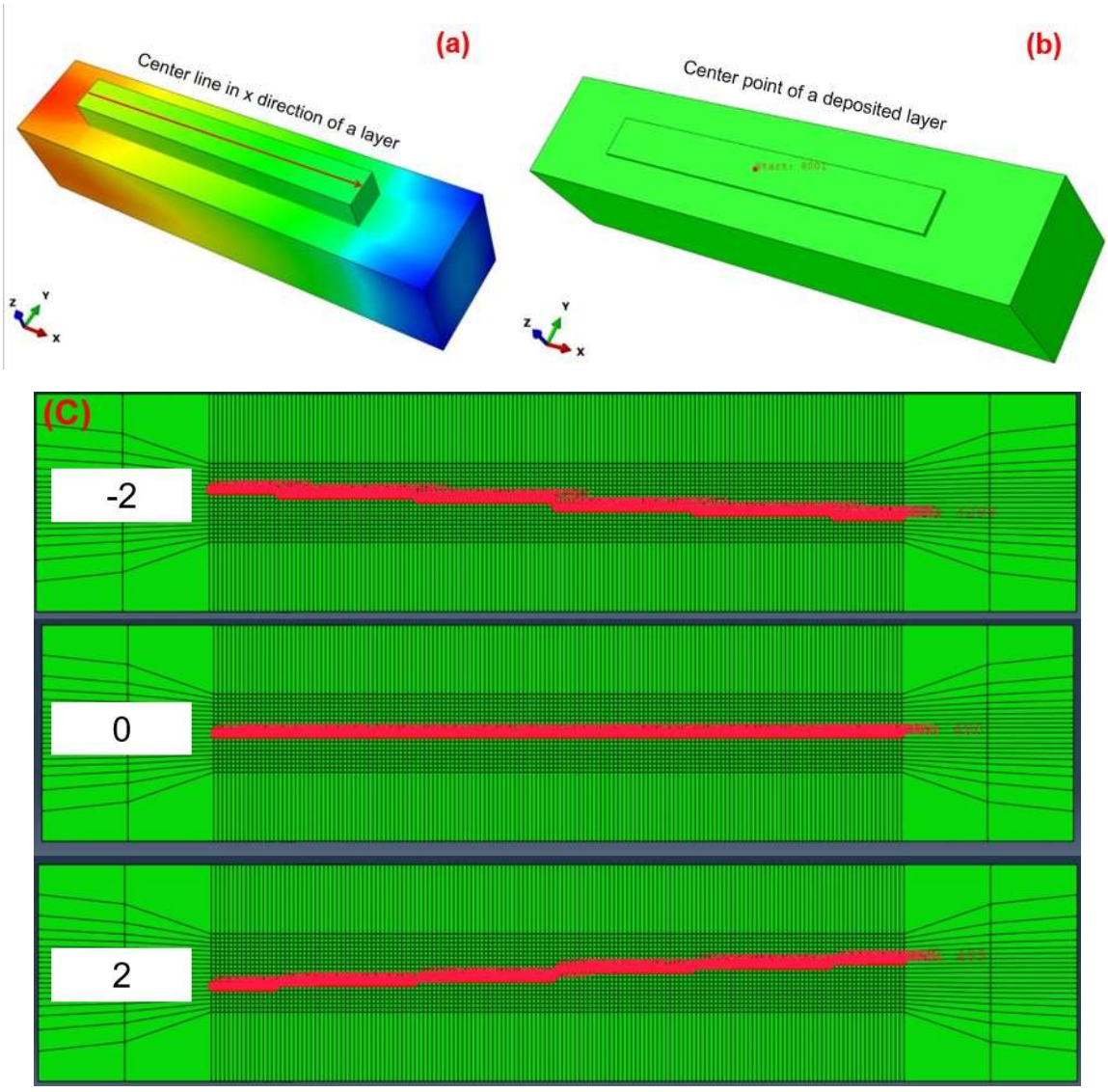

Fig. 3. *Data collection strategy. (a) The inner layer data is collected along the center line in x direction of the layer. (b) The thermal cycle data is collected at the center point of the first deposited layer throughout the deposition. (c) Longitudinal elastic residual strain data is collected respective to different diffraction angle*

2.2 Experimental analysis

The experiments in this work involve the EDD (energy dispersive x-ray diffraction) measurements and the confocal microscopy. The EDD measurement provides the residual strain result inside the samples. The confocal microscopy generates 3D images of the sample for measuring the volume of defects and excessive material deposited.

2.2.1 EDD measurements

Energy dispersive diffraction (EDD) is used to experimentally measure the residual strain of the GRCop-42 samples. EDD is a technique used to study the crystal structure of the materials, and it has two types of analysis: energy dispersive x-ray diffraction (EDXRD) and energy dispersive neutron diffraction (EDND). In this work, EDXRD is performed on the samples at Cornell High Energy Synchrotron Source (CHESS). In EDXRD, a multi-wavelength beam of x-ray from synchrotron hits the sample. The beam is diffracted by the sample, and the scattered x-ray is measured to provide the information of crystal structure of the material, such as lattice spacing.

The EDXRD setup is shown in Fig. 4, including an upstream optical table where the incident x-ray beam comes from, a sample table with rotation axis that enables the sample to rotate at a fixed angle 2θ ranging from -2° to 2°, and a detector table that collects the scattered x-rays. When the x-ray is diffracted by the sample, a spectrum is generated where there are distinct peaks of intensity at specific energy levels of photons. The Bragg's law is used to calculate the energy at different peaks, as described by Eq. (9):

$$E = \xi [d \cdot sin(\theta)]^{-1} \tag{9}$$

$$\xi = 0.5hc \tag{10}$$

$$d = \lambda[2sin(\theta)]^{-1} \tag{11}$$

Here E is photon energy with the unit of keV; ξ is EDD constant with a value of 6.1993 keVÅ; $h\ is$ Planck's constant; c is speed of light; d is the interplanar spacing; θ is the diffraction angle; λ is the wavelength of x-ray beam.

Shifts in the position of intensity peaks are used to measure the internal elastic strains of the sample, as illustrated by Eq. (12):[23]

$$\varepsilon = \frac{d-d_0}{d_0} = \frac{E_0-E}{E_0} \tag{12}$$

$$E_0 = 12.398/\lambda \tag{13}$$

$$\lambda = 2d_0 sin(\theta) \tag{14}$$

Here E_0 and d_0 are the reference energy and lattice spacing calculated from a cubic GRCop-42 specimen. This cubic sample has its internal forces released, which in theory is perfectly stress-relieved and has zero strain. The d_0 value is initially unknown for GRCop-42. It is manipulated to calculate the strain in the cubic sample, and it is determined when the strain value measured in the cubic sample is closest to zero. With the reference E_0 and d_0, the residual elastic strain represented by the ε_{11} strain component is calculated and analyzed.

While calculating the photon energy, E, peak fitting method is applied at the intensity peak of interest. In this work, three different peak fitting methods are utilized: single strain, robust and least squares. For each scan, the energy intensity data is fitted with all three methods. The normalized root mean squared error of each method is compared to choose best fit for that

specific scan. The least square method provides the credible data fitting for most of the scans with an average error of 3.44%. Same procedure of peak fitting is applied to all the energy intensity data collected from different diffraction angle. And the error of residual strain result is mainly caused by the error from the intensity peak fitting.

The shift in [3,1,1] energy intensity peak is utilized to calculate the residual elastic strain using Eq. (12). There are two reasons for choosing this specific peak. First, the [3,1,1] peak is observed to be an isolated peak with no overlap with other peaks. The energy intensity in this peak has a high contrast to the background. Therefore, the corresponding photon energy can be easily achieved from the energy intensity spectrum. Second, at a high diffraction angle, even a small change in lattice spacing can be observed as a huge change in the shift of intensity peak. Therefore, [3,1,1] is picked for the residual strain calculation.

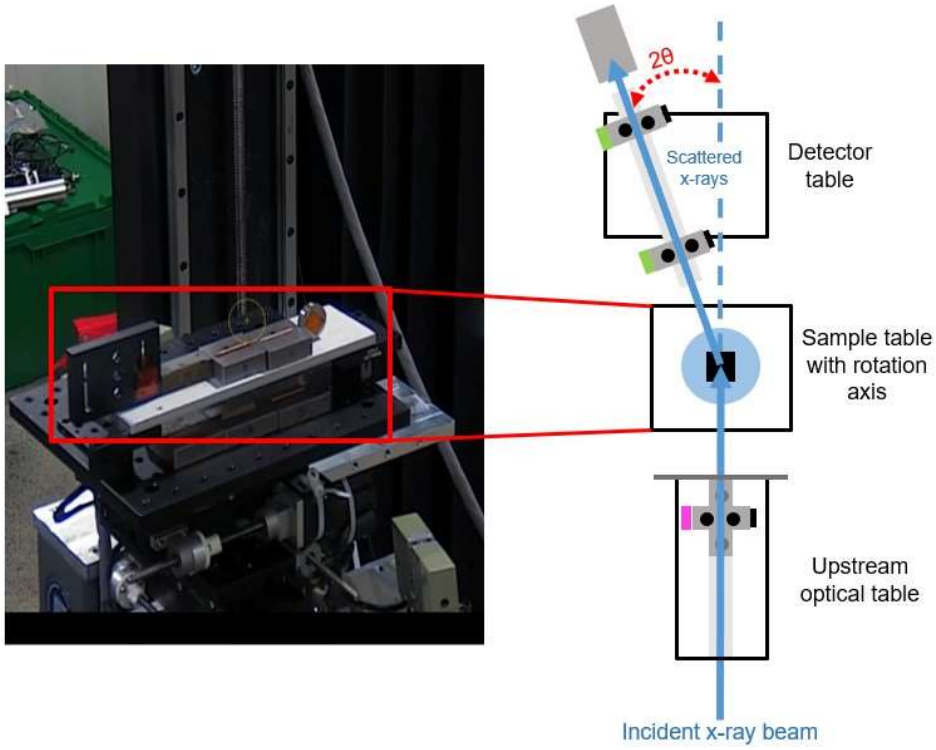

Fig. 4. *Energy Dispersive X-ray Diffraction setup. The incident x-ray beam and the scattered x-ray are represented in the blue solid line. The diffraction angle* 2θ *is noted in red color, and it indicates the angle between the incident and scattered x-ray beam.*

2.2.2 EDD scan strategy

The EDD scan strategy of 8-layer sample is demonstrated in Fig. 5. Each red square represents a 0.2mm x 0.2mm scan spot on the sample, which efficiently covers the thickness of a single layer. The position of scan spots on the left-most and right-most columns are firstly defined after the alignment by a Keyence laser. There exists a gap between the real edge of the sample and the outer boundary of scan spots. For each scan spot, the sample is rotated with an angle 2θ. Here, the angle 2θ represents the angle between the incident and the scattered x-ray beam, in other words, diffraction angle. 21 values of 2θ are picked in the range of -2° to 2° with an equal interval of 0.2°. The purpose for scanning with different diffraction angles is to eliminate the error induced by texture of the sample. When the sample has texture, some specific intensity peak can be observed at one 2θ value but disappear at another 2θ value. The intensities of various peaks would also fluctuate a lot because of texture. After averaging the energy intensity data collected from all different diffraction angles in the -2° to 2° range, all of the intensity peaks can be observed, and a more holistic view of the sample can be achieved.

In each layer, 8 overlapped scan spots are taken on both left and right end of the sample. In the top (8^{th}), middle (4^{th}) and bottom (1^{st}) layers, 7 evenly spaced scan spots are implemented to measure the strain value throughout the layer. The purpose of taking more scans on the edges is to capture the frequent change in residual stress due to the steep shift of temperature on the left and right ends layer by layer. Similar like 8-layer sample, the 2 layers and 5 layers sample use the same scan strategy. A 2D map of residual strains for each sample is produced.

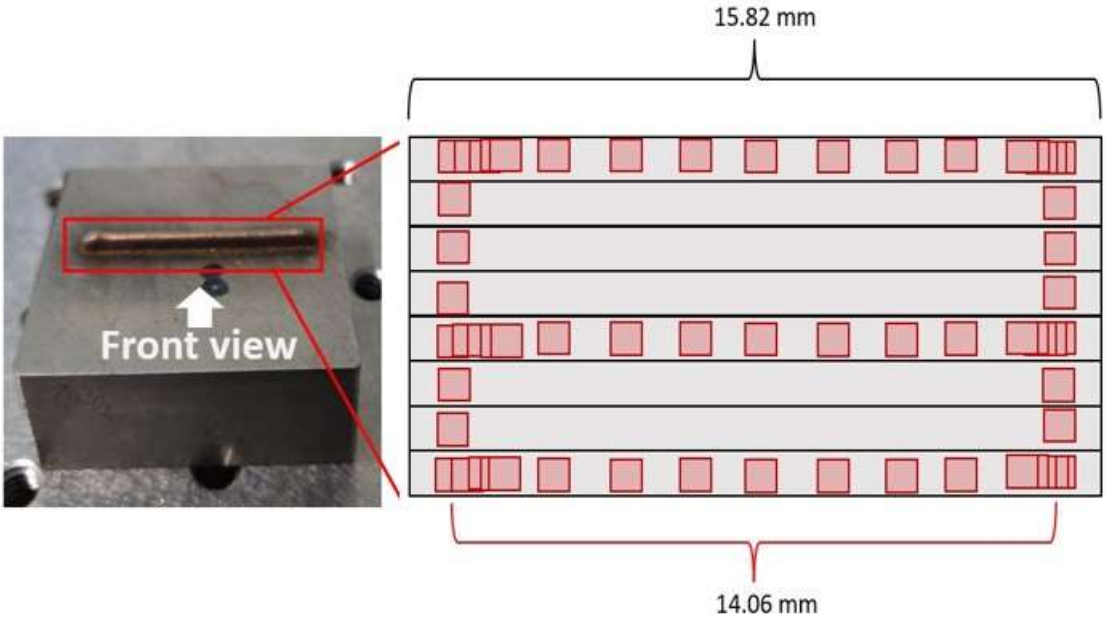

Fig. 5. *Schematic of EDD scan strategy for the 8-layer sample. Each red square represents a spot where an EDD scan is performed on the sample. Multiple overlapped scan spots are picked on the edges to capture the residual strain change between layers. The 7 evenly spaced scan spots measure the inner layer residual strain development. The gap between sample edge and the scan spots near the edge is about 0.8mm.*

2.2.3 Confocal Microscopy

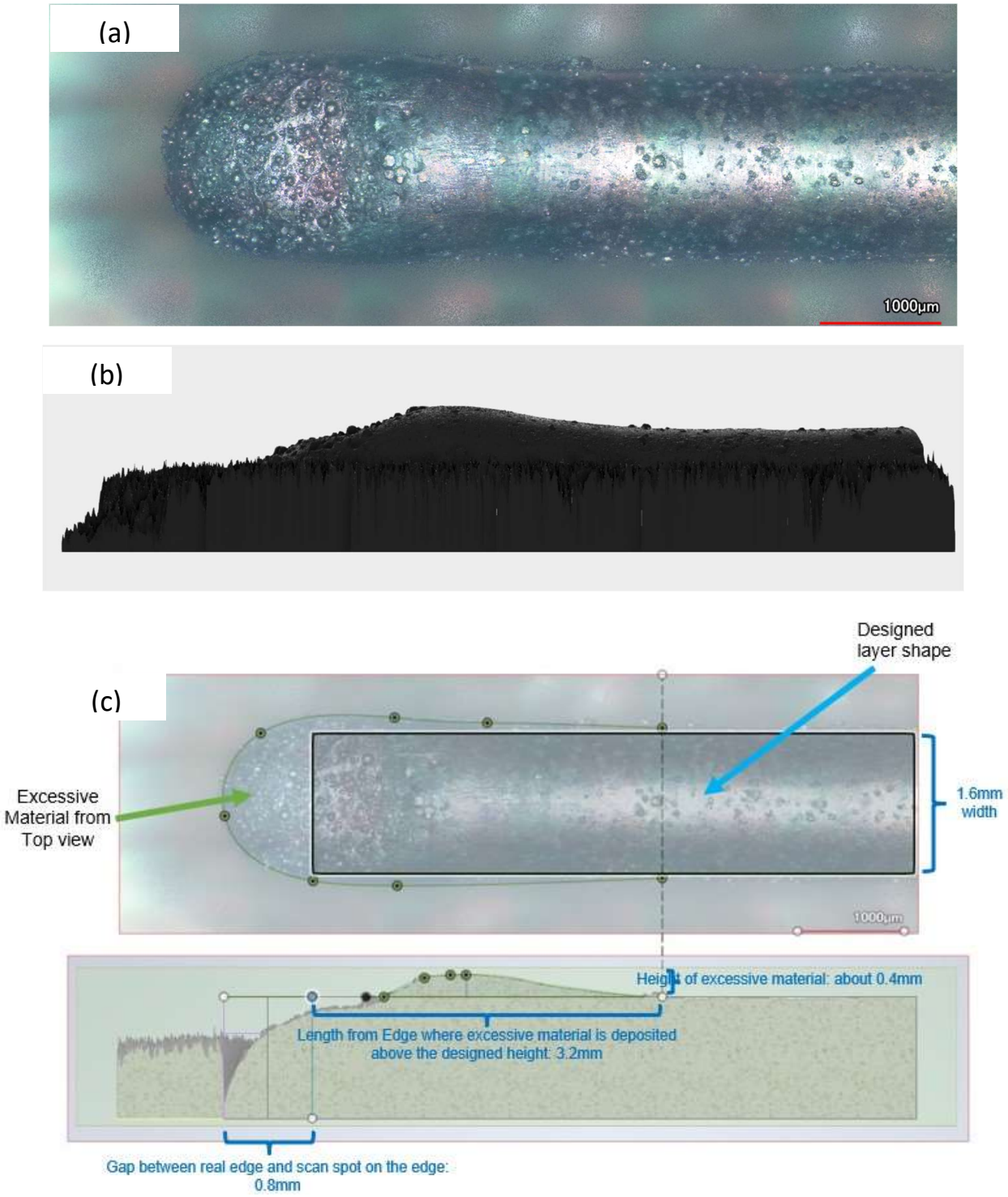

Fig. 6. *Confocal microscopy of the left edge in the 8-layer sample. (a) Optical image. (b) 3D model obtained from confocal microscopy. (c) Measurement of excessive material deposited on left edge using the center-cut view of 3D model.*

The confocal microscopy is performed to observe the irregular shape on the edges and to measure the excessive material deposited on the edge of sample. The confocal laser scanning microscope allows for a comprehensive 3D representation of the microstructure with high resolution [37]. In this work, the confocal microscopy is mainly performed on the edges of the samples. The area scanned on the edges is 20% of the total length of the sample. After the confocal microscopy, a 3D assembly STP file is generated and the area of excessively deposited material on the edges is calculated from the center-cut view of the 3D model. Based on the results from confocal microscopy, the geometry in thermomechanical model is updated to test the change in residual stress when the corner of sample is rounded and protuberant.

CHAPTER THREE

Result and Discussion

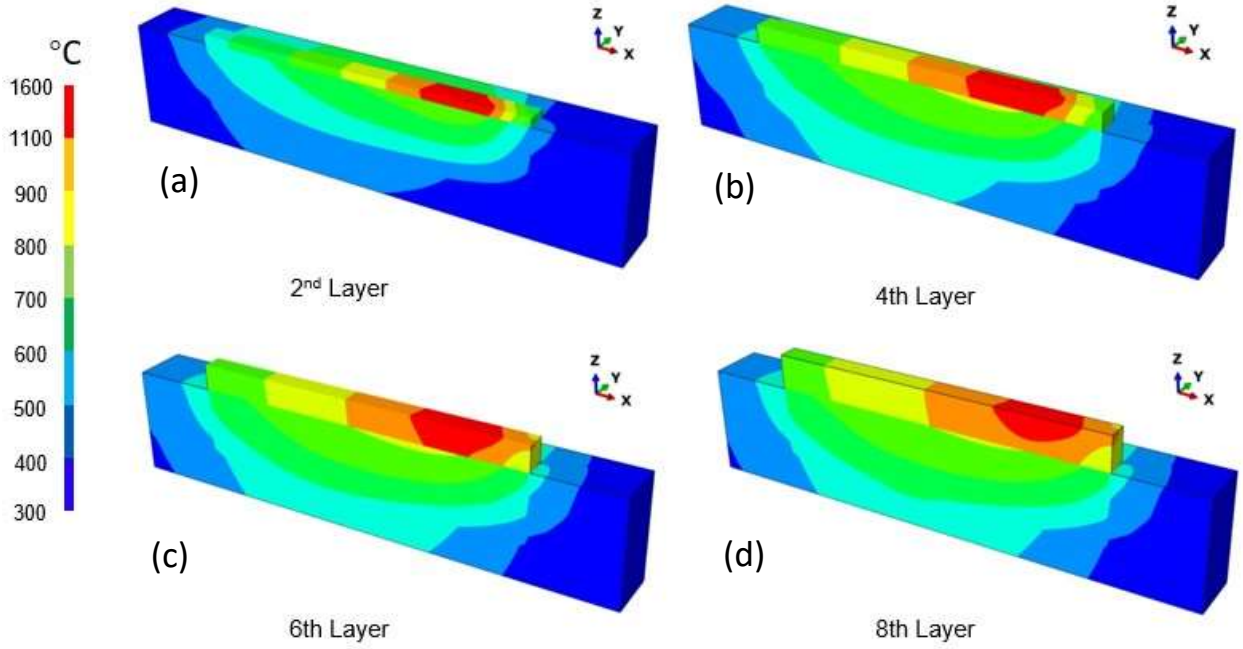

Fig. 7. *Thermal history of the (a) 2nd (b) 4th (c) 6th and (d) 8th layer for the 8-layer sample. The data is collected right after the end of deposition for that specific layer*

3.1 Temperature history

Fig. 7 shows the computed temperature history of the 8-layer GRCop-42 sample when the material deposition has just been completed at 2nd, 4th, 6th and 8th layer. The color bar on the left represents the temperature range, where the red color indicates region with temperature above 1100°C, melting point of GRCop-42. The melt pool size is illustrated by the red ellipsoid shape in each graph. The temperature peak appears at the center of the melt pool, and the temperature around the melt pool decreases progressively. By observing the development of melt pool at different layers, it is shown that the melt pool spans across multiple layers of deposited material. This indicates that the melt of current layer and the re-melt of the previously deposited

layer happens at the same time. The average layer thickness in this work is only 0.2mm, which is very thin and contributes to the re-melting phenomenon.

Fig. 8(a) shows the temperature development at the center point of the first deposited layer. Each peak in the curve shows the rise of temperature when the laser heat source passes the center point of each layer, and then the temperature drops after the laser moves to the edges. Such rapid change of temperature appears 8 times in the 7 seconds deposition of material, which proves the transient temperature field of the DED process in AM. The ascending temperature at each peak indicates the fact that the heat is accumulated during the deposition. The same fact is also proved by the temperature history of each layer during the deposition of the 8-layer sample, as shown in Fig. 10(a). Here the 8^{th} layer is the top layer and 1^{st} layer is the bottom layer. The lines in the plot depict the temperature at the centerline of each layer right after the deposition of that specific layer is finished. The temperature curve shows a higher value at the right end because the laser heat source moves from left to right, and the data is collected when the laser just left from the right edge.

From the bottom to top layer, the peak temperature increases from 1100°C to 1600°C. Two reasons for the heat accumulating and exceeding the melting temperature of GRCop-42 can be declared here. First, as mentioned in section 2.1, the material and heat loss due to phase change is ignored in this thermomechanical model. The energy required for the phase change continuously contributes to the rise of temperature. Second, the substrate absorbs the heat input from the laser heat source, and its temperature also increases during the deposition. At higher levels, the temperature difference between the deposited layer and substrate is much smaller than that at the beginning. The heat conduction from layers to substrate is weaker at higher layer, as the result, the heat is more likely to accumulate when the layer goes higher. At lower layers, the

temperature difference between substrate and deposited layer is very huge, the high heat conduction rate limits the temperature increase. The cross of temperature line for 1st and 2nd layer can be clearly explained by this reason. The significant variation and rapid change in temperature lead to the formation of residual stress and strain fields.

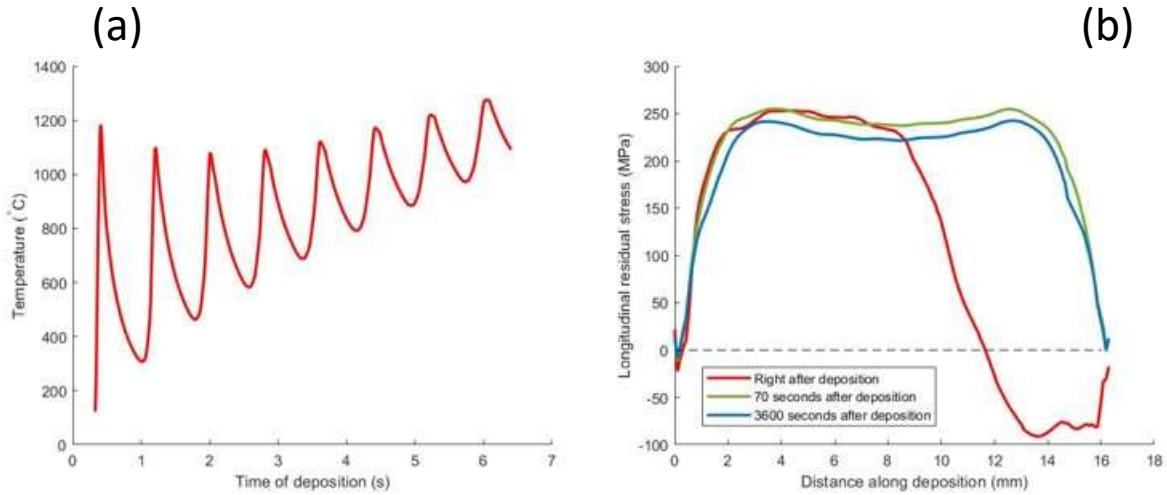

Fig. 8. *(a) Thermal cycle of 8-layer samples (b) Residual stress on the middle layer during the cooling process*

3.2 Modeled residual stress and strain

Fig. 9 shows the longitudinal residual stress and residual elastic strain development during the material deposition. The data is collected at the end of the deposition of 2nd, 4th, 6th and 8th layer. Positive residual stress and residual elastic strain value indicate tensile component, and the negative value indicates compressive component. The longitudinal stress and strain component, σ_{11} and ε_{11}, are measured because the longitudinal residual stress is proved to have significant influence on crack propagation, buckling and distortion [38-40]. It is shown that the maximum residual stress and residual elastic strain appears at the center when the layer is low, and they move to the top of the deposited layers as the layer goes higher. One essential observation can be made from the result of 6th and 8th layer is that the compressive residual stress

emerges at the top area of right half, and bottom layers have the tensile stress. This stress distribution can be explained by the melt pool development shown in Fig. 7. For example, when the deposition of 8^{th} layer has just been finished, the melt pool appears in the top 4 layers because of the remelting effects. The lower layers on the right half are still in solid state. During the material deposition, the laser heat source heats up the deposited material quickly and causes the thermal expansion, but such expansion is restrained by the surrounding material with lower temperature. Therefore, a compressive residual stress is formed in the heated zone. In contrast to that, the tensile residual stress is formed during the cooling and solidification because of the shrinkage of material.

In this case, the material inside the melt pool on the top layers tends to cool down and to solidify, which brings the tensile residual stress inside the layers. The material at bottom layers is heated up when the laser passes over the right edge. At the same time, it receives the heat emitted from top layer due to the solidification. As a result, the compression residual stress is formed at the lower layers on the right half. The massive tensile residual stress on the left half is because the laser moves so far that it has no heating effect on this area. The deposited material starts to cool down and causes the tensile stress.

The development of residual elastic strain follows the same explanation. Although this simulation is conducted with a maximum of 8 layers, the fact of higher layer subjects to higher residual elastic strain can still be proved. The lower residual elastic strain is observed at bottom layers. And the peak temperature continuously increases as the layer goes higher, which causes a drastic temperature variation between top and bottom layers. All the above factors will add to a higher residual elastic strain on the upper layers.

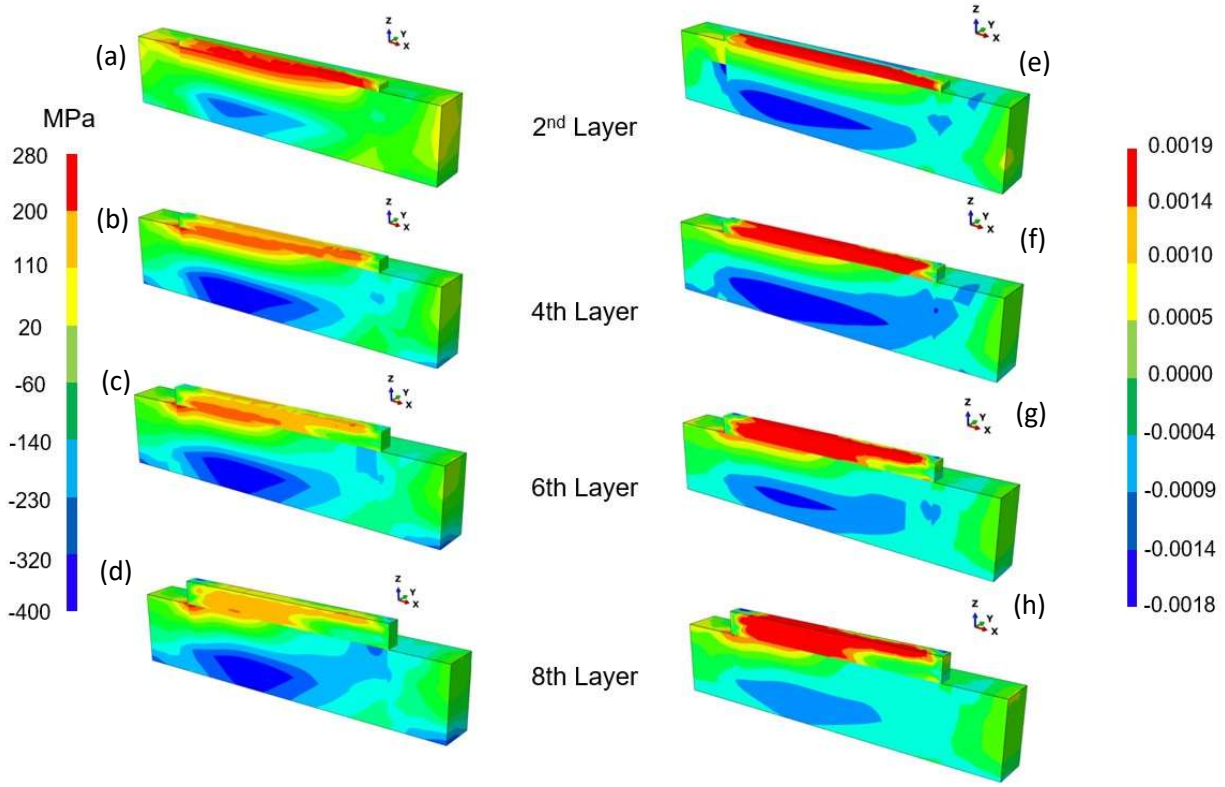

Fig. 9. *Longitudinal residual stress of (a) 2nd (b) 4th (c) 6th and (d) 8th layer for the 8-layer sample, and the longitudinal residual elastic strain of (e) 2nd (f) 4th (g) 6th and (h) 8th layer for the 8-layer sample*

Fig. 10(b) shows the residual stress of each layer. Similar to temperature history in Fig. 10(a), residual stress data is collected at the centerline of each layer right after that layer finished deposition. The residual stress of the first three layers is observed to be higher than the other layers. The reason for that is when the deposition starts in the first several layers, the temperature of the substrate is still low. The huge temperature difference between the cold substrate and the hot deposited material leads to the high residual stress. The residual stress on the very end of left and right edge are close to zero, which shows that the elements on the edge of the samples are mostly stress free. The area near the edges, such as 1mm to 3mm and 13mm to 15mm, shows a higher residual stress than the middle section. This is because the edge of deposited layers

solidifies much sooner than the middle area. When the middle area starts to solidify, the material shrinkage causes the higher tensile stress on the edges.

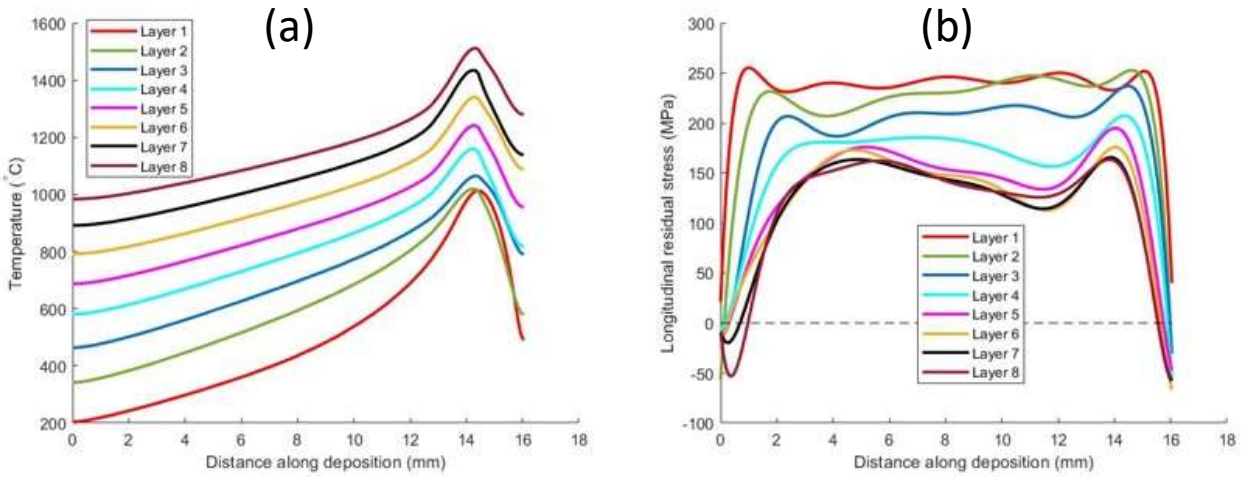

Fig. 10. *Development in (a) temperature and (b) residual stress for each layer in the 8 layer sample. Data is collected right after deposition is finished for that specific layer*

Fig. 8(b) describes the residual stress development of the middle (4^{th}) layer during the cooling process. At 0 seconds, the deposition of all the layers has just been finished. At this moment, the laser heat source just leaves the right edge of the 8th layer, and the formation of melt pool is ongoing because of high temperature. The residual stress on the right edge tends to be compressive. As time progresses, the residual stress field also develops. At 70 seconds, the temperature decreases to 200°C and the residual stress appears to be tensile during the cooling process. After 3600 seconds, the temperature of deposited materials fully reduces to 25°C, the room temperature. The stress magnitude slightly increases and nearly all the residual stress is tensile.

3.3 Experimental residual strain and result comparison

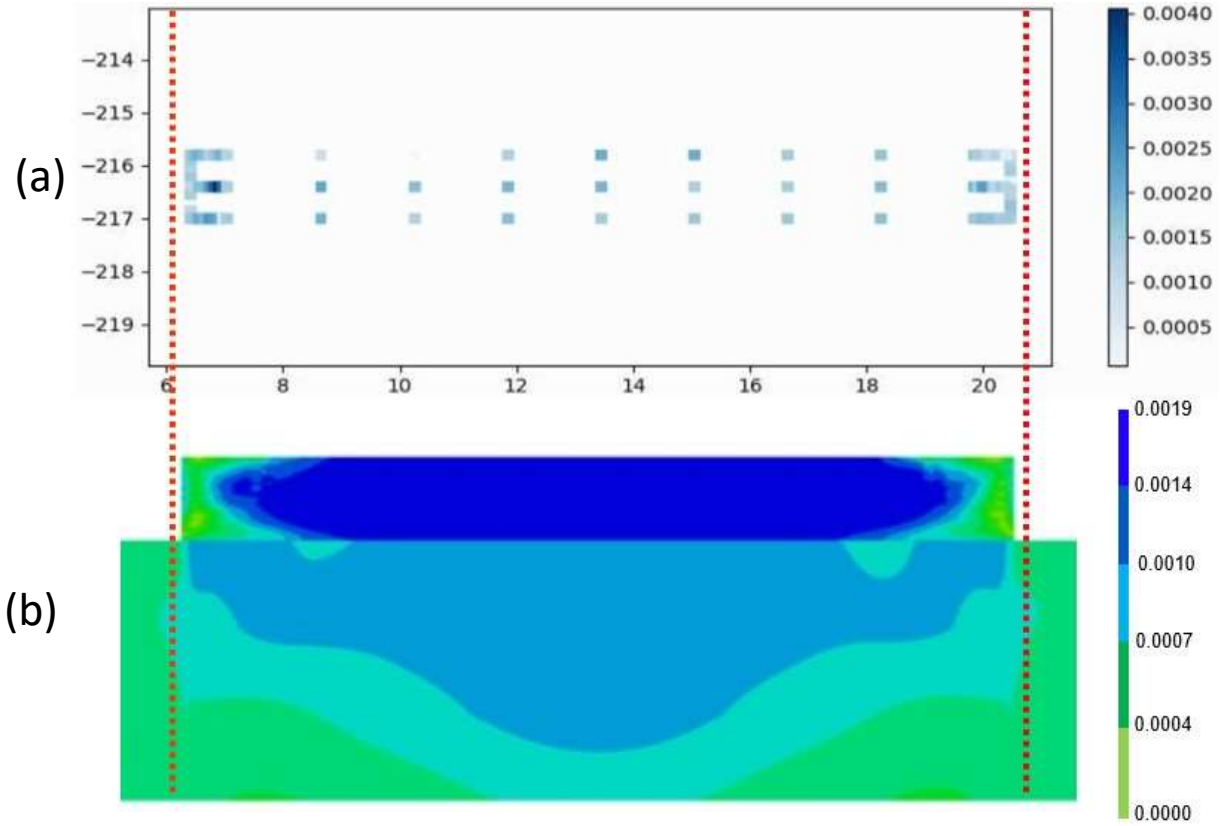

Fig. 11. *The comparison between the residual strain results from (a) EDD and (b) simulation. The blue dots in EDD result represent the residual strain value of the deposited material. The shade of blue shows the magnitude of strain. The coordinates on the vertical and horizontal axis are the reference position in EDD experiment. The strain value in simulated result is represented by the color in greens and blues.*

Fig. 11(a) shows the residual elastic strain result from experimental EDD analysis, and Fig. 11(b) shows the similar result from the thermomechanical simulation. The EDD analysis is performed after the sample totally cools down to the room temperature. The elastic residual strain result obtained from EDD analysis is longitudinal because the diffraction angle in EDD experiment ranges from -2 degrees to 2 degrees. The longitudinal residual strain can be achieved at lower diffraction angles. With 21 values of diffraction angles in each scan spot, the intensity data is averaged and the shift in the intensity peaks is observed to calculate the longitudinal

elastic residual strain. The blue color represents the tensile residual elastic strain. It can be seen that almost all the scan spots display a tensile elastic strain. As explained in section 4.2, the material shrinkage during cooling process results in the formation of tensile strain. An asymmetry is observed from the elastic strain value at left and right ends. This indicates that the residual stress developments on the edges are different, which is caused by the imperfect rectangular geometry on the edges.

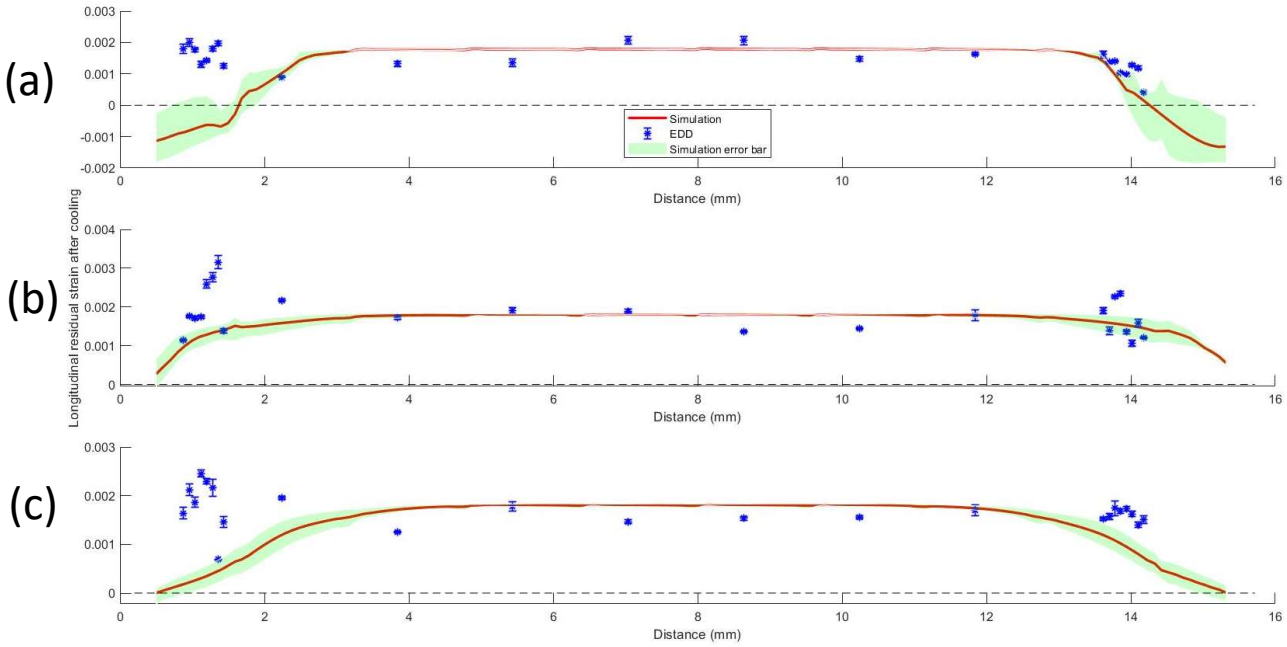

Fig. 12. *Longitudinal residual Strain results of (a) 8th (b) 4th and (c) 1st layers for 8-layer sample by EDD analysis and simulation. The result from the simulation is depicted by the red lines. The error of the simulated result is covered by the green area. The EDD result is represented by the blue stars with an error bar. The error source of EDD result comes from the peak fitting of energy intensity data.*

Fig. 12 shows the comparison of residual strain value between the EDD result and simulation result. The comparison is made for top, middle, and bottom layer of the 8-layer sample. The longitudinal elastic residual strain calculated from the simulation is depicted by the red lines. It is the average result from the data collected in different diffraction angles, as shown in the Fig. 3. As presented in the Fig. 12, the middle section from 2mm to 14mm shows a good

agreement between the simulated and experimental result for all layers. However, the strain magnitude on the edges exhibits a little difference, especially on the left edge. The simulation result gives a slightly lower strain value on the left edge. One of the most possible reason is the geometry difference between the simulation model and the real sample. In the thermomechanical model, the geometry of deposited layer is set to be a perfect rectangular block; however, the 3D model of the manufactured sample created from confocal microscopy shows that the bulging corner on the edges. During the deposition of material, the material inside the melt pool is in the liquid state. The surface tension of the liquid metal causes the round shape of the front boundary of melt pool. Therefore, when the materials on the edge start to solidify, the geometry of the edges are frequently rounded. By observing the 3D model for the left edge in 8-layer sample, it is found that the height of edge is higher than the other area, which indicates an excessive material deposition. The measurement shows the extra material on the left edge with a volume of 3.2mm x 0.4mm x 0.16mm. The geometry of thermomechanical model is revised using two approaches. In approach one, the extra material is placed in the extra layers over the top of the previous geometry. In approach two, the excessive material is averaged to layers, and the geometry of each layer is changed to reproduce the bulging corner. The updated longitudinal elastic residual strain result of each approach is shown in Fig. 13.

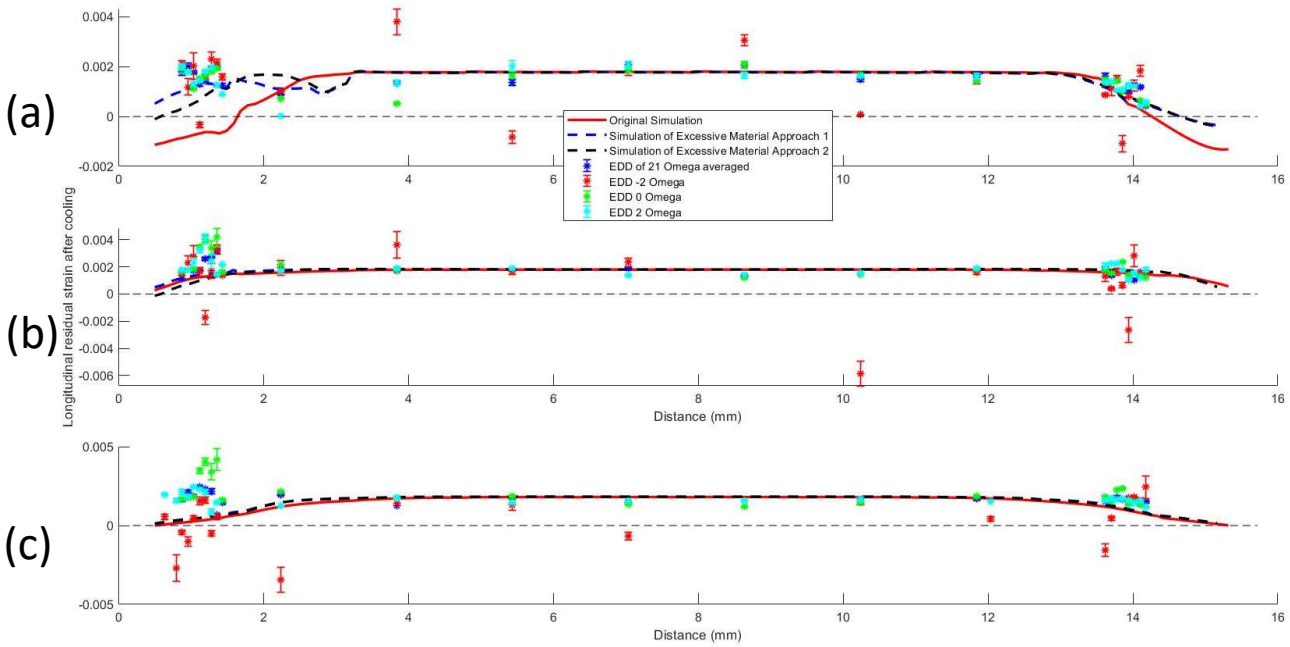

Fig. 13. *The updated longitudinal residual strain result of (a) 8th (b) 4th and (c) 1st layers for 8-layer sample. The original result from the simulation is depicted by the red line. The updated strain result is described by the black and blue dashed line. The EDD result is represented by the stars with an error bar. Different Omega values represent different x-ray diffraction angle*

The updated thermomechanical model successfully captures the influence on residual strain by excessive material at the left edge for the top layer. The updated residual strain result of 8th layer using both approaches shows a curve-up that approaches EDD result on the left edge, but the strain value of 4th and 1st layer remains almost the same. Because the excessive material deposited on the left acts like an extra layer, as discussed in section 4.2, higher residual strain is inclined to appear on the higher layers. The other reason for the discrepancy between the simulated and experimental result can be the error introduced by the assumption used in the thermomechanical model.

From the simulation, the longitudinal elastic strain approaches zero at the end of edges. But the EDD experiment is not able to obtain the strain value on the very end of the edges. Due to the gap between the sample's real edge and the left-most and right-most EDD scan spots, the

EDD experiment is only able to get the strain value near the edges, but not exactly on the edge. This explains the discrepancy at the very end of the edges. Overall, the simulation model successfully captures the trend of residual stress development on the edges.

3.4 AM Parameter study with thermomechanical model

After the validation by comparing the simulation results and EDD results, the thermomechanical model is tested to be reliable in predicting the residual stress development in the additive manufacturing process. The study about the influence of different laser parameters and material properties is conducted with this simulation model. The simulations are performed on the 2 layer sample, and the residual stress result is collected along the center line of the top layer after the sample cools down to the room remperature.

Firstly multiple laser power and scanning speed are tested. Only one laser parameter is altered in each simulation, and the process window of GRCop-42 is ensured while changing the parameters. As shown in Fig. 14, different laser power and scanning speed have some level of impact on the residual stress development. Increasing the scanning speed and decreasing the laser power both decrease the residual stress. 10% of residual stress is reduced in the middle section, and greater effect is observed on the edges with a 35% reduction of residual stress. In a certain time of deposition, either redusing the laser power or increasing the scanning speed lower the total heat input received by the material during the deposition process, which results in a smaller temperature gradient between the layers, especially on the edges. Consequently, the residual stress decreases with a faster scanning speed and lower laser power.

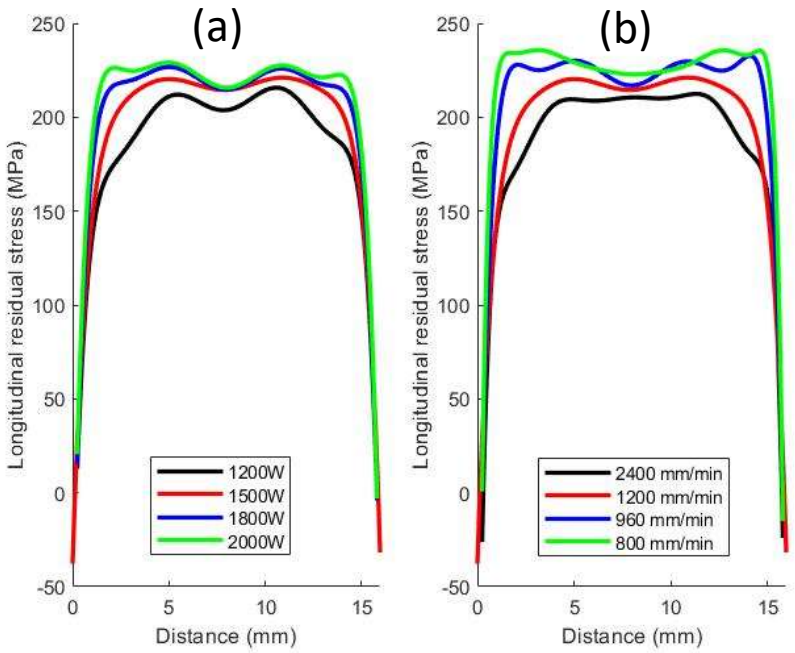

Fig. 14. *The evolution of residual stress under different laser processing parameters. (a) Laser power (b) Laser scanning speed. The simulations are performed on the 2 layers sample. The longitudinal residual stress data is collected along the center line in x direction of the top layer.*

Different material properties, including yield strength, thermal expansion coefficient and laser absorptivity, are tested to assess their influence on residual stress. The material properties for comparison are derived from the commonly used material in additive manufacturing. For example, sensitivity test of yield strength is performed using the values from selective laser melting and laser powder bed fusion manufactured GRCop-42. In each simulation, only one of the material properties is changed, others remain the same. Fig. 15(a) shows the residual stress development of the materials with different yield strength. The residual stress of higher yield strength material is much higher, and lower yield strength results in a lower residual stress. However, both residual stress and the yield strength determine whether the cracks and distortion occur on the manufactured parts. Therefore, a normalized stress calculated by the ratio of yield stress and residual stress of the material is presented in the Fig. 15(b). The material with stronger

yield strength has a slightly higher normalized stress curve at both ends, which means that it is more likely to have distortion and cracks. In other words, stiffer materials are susceptible to higher residual stress. Therefore, the material selection in additive manufacturing should not only consider its mechanical properties but also take the residual development into account.

Similar simulation is performed on different thermal expansion coefficient and laser absorptivity. The lower thermal expansion coefficient is picked from stainless steel, and the higher laser absorptivity of 40% is chosen from the data of pure copper under the laser with 515nm wavelength[41]. The Fig. 15(c) and 15(d) present that the material with lower thermal expansion coefficient is subjected to a slightly lower residual stress. The laser absorptivity does not significantly affect the residual stress. Overall, the yield strength has the highest impact on residual stress development with respect to other material properties and processing parameters. This thermomechanical model provides an effective tool for the future parameter studies.

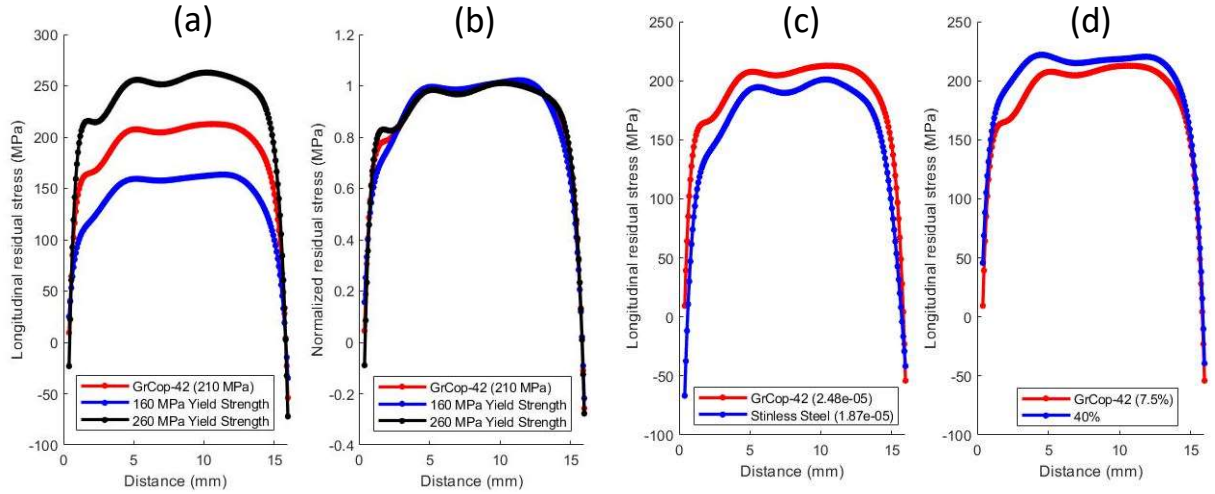

Fig. 15. *The evolution of residual stress under different material properties. (a) yield strength (c) thermal expansion coefficient and (d) laser absorptivity. (b) shows the normalized stress calculated by the ratio of yield stress and residual stress. The simulations are performed on the 2 layers sample. The longitudinal residual stress data is collected along the center line in x direction of the top layer.*

CHAPTER FOUR

Conclusions

The residual stress development and temperature history of DED manufactured GRCop-42 sample is simulated with the thermomechanical model. The residual strain of the sample is experimentally measured using EDD. The comparison between simulated result and experimental result validates the reliability of such predictive model. The influence of different laser parameters and material properties on the residual stress development in the DED process is explored. The conclusions from this work are listed below:

- The melting and remelting of the material happen simultaneously. The transient temperature field and the steep temperature gradient lead to the formation of residual stress and strain fields.
- The thermomechanical simulation successfully modeled the residual stress development of the DED process. The formation of compressive residual stress happens during the heating process, and the tensile stress appears in the cooling process. The residual strain tends to be higher at the upper layers. The edges of a deposited layer are subject to higher residual stress than the middle section.
- Both the EDD measurement result and the simulated result show a completely tensile strain over the deposited layers. A good agreement of the strain value in middle section is confirmed, but a mismatch of results is observed on the left edge. The discrepancy is explained by the excessive material deposited on the bulging edges.
- The parameter study is conducted by testing the influence of different laser parameters and material properties on the development of residual stress. The laser power and

scanning speed have a certain extent of influence on the residual stress as changing these parameters affects the total heat input to the deposited layer. Yield strength is one of the most influential properties on the residual stress. The material with higher yield strength is susceptible to higher residual stress. The thermal expansion coefficient and laser absorptivity of material are proved to have slight impact on residual stress.

In general, the simulation model does a good job predicting the residual stress development DED process. Some future work might be conducted to improve the performance of this model, such as improving the element birth accuracy. It is hoped that such a predictive model will help analyzing the residual stress to enhance the performance of metal additive manufacturing in a wide range of industrial applications.

REFERENCE

[1] M. A. Khan, A. Latheef, Metal additive manufacturing of alloy structures in architecture: A review on achievements and challenges, Materials Today: Proceedings (2023) ISSN 2214-7853, https://doi.org/10.1016/j.matpr.2023.05.192.

[2] M. Armstrong, H. Mehrabi, N. Naveed, An overview of modern metal additive manufacturing technology, Journal of Manufacturing Processes, Volume 84 (2022) Pages 1001-1029, ISSN 1526-6125, https://doi.org/10.1016/j.jmapro.2022.10.060.

[3] F. Günther, S. Pilz, F. Hirsch, M. Wagner, M. Kästner, A. Gebert, M. Zimmermann, Shape optimization of additively manufactured lattices based on triply periodic minimal surfaces, Additive Manufacturing, Volume 73, 2023, 103659, ISSN 2214-8604, https://doi.org/10.1016/j.addma.2023.103659.

[4] M. L. Dezaki, A. Serjouei, A. Zolfagharian, M. Fotouhi, M. Moradi, M.K.A. Ariffin, M. Bodaghi, A review on additive/subtractive hybrid manufacturing of directed energy deposition (DED) process, Advanced Powder Materials, Volume 1, Issue 4 (2022) 100054, ISSN 2772-834X, https://doi.org/10.1016/j.apmate.2022.100054.

[5] K. Li, W. Chen, N. Gong, H. Pu, J. Luo, D. Z. Zhang, L. E. Murr, A critical review on wire-arc directed energy deposition of high-performance steels, Journal of Materials Research and Technology, Volume 24, 2023, Pages 9369-9412, ISSN 2238-7854, https://doi.org/10.1016/j.jmrt.2023.05.163.

[6] C. Ji, K. Li, J. Zhan, S. Bai, B. Jiang, L. E. Murr, The effects and utility of homogenization and thermodynamic modeling on microstructure and mechanical properties of SS316/IN718 functionally graded materials fabricated by laser-based directed energy deposition, Journal of Materials Processing Technology, Volume 319, 2023, 118084, ISSN 0924-0136, https://doi.org/10.1016/j.jmatprotec.2023.118084.

[7] E. Kim, C. Lee, D. Kim, Study on the characteristics of functionally graded materials from Ni-20cr to Ti-6Al-4V via directed energy deposition, Journal of Alloys and Compounds, Volume 955, 2023, 170263, ISSN 0925-8388, https://doi.org/10.1016/j.jallcom.2023.170263.

[8] A.D. Iams, T.J. Lienert, D.A. Otazu, M. Ramoni, Effects of deposition sequence on microstructural evolution in additively manufactured Cu-Cr-Nb alloy / superalloy bimetallic structures, Additive Manufacturing Letters, Volume 6, 2023, 100151, ISSN 2772-3690, https://doi.org/10.1016/j.addlet.2023.100151.

[9] Li, L., Zhang, X., Cui, W. et al. Temperature and residual stress distribution of FGM parts by DED process: modeling and experimental validation. Int J Adv Manuf Technol 109, 451–462 (2020). https://doi.org/10.1007/s00170-020-05673-4

[10] E. J. Schwalbach, S. P. Donegan, M. G. Chapman, K. J. Chaput, M. A. Groeber, A discrete source model of powder bed fusion additive manufacturing thermal history, Additive

Manufacturing, Volume 25 (2019) Pages 485-498, ISSN 2214-8604, https://doi.org/10.1016/j.addma.2018.12.004.

[11] M. Roy, O. Wodo, Data-driven modeling of thermal history in additive manufacturing, Additive Manufacturing, Volume 32 (2020) 101017, ISSN 2214-8604, https://doi.org/10.1016/j.addma.2019.101017.

[12] H. Chae, E. Huang, W. Woo, S. H. Kang, J. Jain, K. An, S. Y. Lee, Unravelling thermal history during additive manufacturing of martensitic stainless steel, Journal of Alloys and Compounds, Volume 857 (2021) 157555, ISSN 0925-8388, https://doi.org/10.1016/j.jallcom.2020.157555.

[13] S. Chen, H. Gao, Y. Zhang, Q. Wu, Z. Gao, X. Zhou, Review on residual stresses in metal additive manufacturing: formation mechanisms, parameter dependencies, prediction and control approaches, Journal of Materials Research and Technology, Volume 17 (2022) Pages 2950 2974, ISSN 2238-7854, https://doi.org/10.1016/j.jmrt.2022.02.054.

[14] J.R. Hönnige, P.A. Colegrove, B. Ahmad, M.E. Fitzpatrick, S. Ganguly, T.L. Lee, S.W. Williams, Residual stress and texture control in Ti-6Al-4V wire + arc additively manufactured intersections by stress relief and rolling, Materials & Design, Volume 150 (2018) Pages 193-205, ISSN 0264-1275, https://doi.org/10.1016/j.matdes.2018.03.065.

[15] C. Li, Z.Y. Liu, X.Y. Fang, Y.B. Guo, Resodia; stress in metal additive manufacturing, 4th CIRP Conference on Surface Integrity, (2018)

[16] W. Chen, L. Xu, Y. Han, L. Zhao, H. Jing, Control of residual stress in metal additive manufacturing by low-temperature solid-state phase transformation: An experimental and numerical study, Additive Manufacturing, Volume 42 (2021) 102016, ISSN 2214-8604, https://doi.org/10.1016/j.addma.2021.102016.

[17] A. Malmelöv, C. Hassila, M. Fisk, U. Wiklund, A. Lundbäck, Numerical modeling and synchrotron diffraction measurements of residual stresses in laser powder bed fusion manufactured alloy 625, Materials & Design, Volume 216 (2022) 110548, ISSN 0264-1275, https://doi.org/10.1016/j.matdes.2022.110548.

[18] N. Gautam, A. Kumar S., P. R. Mondi, Evaluation methods for residual stress measurement in large components, Materials Today: Proceedings, Volume 44, Part 6 (2021) Pages 4239-4244, ISSN 2214-7853, https://doi.org/10.1016/j.matpr.2020.10.539.

[19] R.H. Leggatt, D.J. Smith, S.D. Smith, Development and experimental validation of the deep hole method for residual stress measurement, J. Strain Anal. Eng. Des. 31 (3) (1996) 177–186.

[20] F. Hosseinzadeh, B. Tafazzoli-Moghaddam, H. K. Kim, P. J. Bouchard, V. Akrivos, A. N. Vasileiou, M. Smith, Residual stresses in austenitic thin-walled pipe girth welds: Manufacture and measurements, International Journal of Pressure Vessels and Piping, Volume 206 (2023) 105016, ISSN 0308-0161, https://doi.org/10.1016/j.ijpvp.2023.105016.

[21] T.Q. Phan, M. Strantza, M.R. Hill, T.H. Gnaupel-Herold, J. Heigel, C.R. D'Elia, A.T. DeWald, B. Clausen, D.C. Pagan, J.Y. Peter Ko, D.W. Brown, L.E. Levine, Elastic Residual Strain and Stress Measurements and Corresponding Part Deflections of 3D Additive Manufacturing Builds of IN625 AM-Bench Artifacts Using Neutron Diffraction, Synchrotron X-Ray Diffraction, and Contour Method, Integr. Mater. Manuf. Innov. 8 (3) (2019) 318–334, https://doi.org/10.1007/s40192-019-00149-0.

[22] O. Takakuwa and H. Soyama, Optimizing the Conditions for Residual Stress Measurement Using a Two-Dimensional XRD Method with Specimen Oscillation, Advances in Materials Physics and Chemistry, Vol. 3 No. 1A (2013) pp. 8-18. https://dpi.org10.4236/ampc.2013.31A002.

[23] M. Croft, V. Shukla, E. K. Akdoğan, N. Jisrawi, Z. Zhong, R. Sadangi, A. Ignatov, L. Balarinni, K. Horvath, T. Tsakalakos, In situ strain profiling of elastoplastic bending in Ti–6Al–4V alloy by synchrotron energy dispersive x-ray diffraction, Journal of Applied Physics 105, 093505 (2009) https://doi.org/10.1063/1.3122029

[24] M.L. Suominen Fuller, R.J. Klassen, N.S. McIntyre, A.R. Gerson, S. Ramamurthy, P.J. King, W. Liu, Texture, residual strain, and plastic deformation around scratches in alloy 600 using synchrotron X-ray Laue micro-diffraction, Journal of Nuclear Materials, Volume 374, Issue 3 (2008) Pages 482-487, ISSN 0022-3115, https://doi.org/10.1016/j.jnucmat.2007.10.015.

[25] P. Chang, T. Teng, Numerical and experimental investigations on the residual stresses of the butt-welded joints, Computational Materials Science, Volume 29, Issue 4 (2004) Pages 511-522, ISSN 0927-0256, https://doi.org/10.1016/j.commatsci.2003.12.005.

[26] H. Zhao, C. Yu, Z. Liu, C. Liu, Y. Zhan, A novel finite element method for simulating residual stress of TC4 alloy produced by laser additive manufacturing, Optics & Laser Technology, Volume 157 (2023) 108765, ISSN 0030-3992, https://doi.org/10.1016/j.optlastec.2022.108765.

[27] F. Montevecchi, G. Venturini, A. Scippa, G. Campatelli, Finite Element Modelling of Wire-arc-additive-manufacturing Process, Procedia CIRP, Volume 55 (2016) Pages 109-114, ISSN 2212-8271, https://doi.org/10.1016/j.procir.2016.08.024.

[28] Goldak, J., Chakravarti, A. & Bibby, M. A new finite element model for welding heat sources. Metall Trans B 15, 299–305 (1984). https://doi.org/10.1007/BF02667333

[29] T. Mukherjee, W. Zhang, T. DebRoy, An improved prediction of residual stresses and distortion in additive manufacturing, Computational Materials Science, Volume 126 (2017) Pages 360-372, ISSN 0927-0256, https://doi.org/10.1016/j.commatsci.2016.10.003.

[30] G. Vastola, G. Zhang, et al., Controlling of residual stress in additive manufacturing of Ti6Al4V by finite element modeling, Addit. Manuf. 12 (2016) 231–239.

[31] O. Fergani, F. Berto, et al., Analytical modeling of residual stress in additive manufacturing, Fatigue Fract. Eng. Mater. Struct. 40 (6) (2017) 971–978.

[32] K.G. Cooper, J.L. Lydon, M.D. LeCorre, Z.C. Jones, D.S. Scannapieco, D.L. Ellis, B.A. Lerch, Three-Dimensional Printing GRCop-42, Technical Memorandum of NASA, Metals and Metallic Materials (2018)

[33] S. Thomas, S. Yazdanparast, O. Hildreth, M. A. Zaeem, Formation energies, electronic properties and elemental diffusion of Cu–Cr–Nb (GRCop) alloys, Physica B: Condensed Matter, Volume 637 (2022) 413909, ISSN 0921-4526, https://doi.org/10.1016/j.physb.2022.413909.

[34] A.H. Seltzman, S.J. Wukitch, Brazing characteristics, microstructure, and wettability of laser powder bed fusion additive manufactured GRCop-84 compared to CuCrZr and OFC, and brazing to titanium-zirconium-molybdenum alloy limiters, Fusion Engineering and Design, Volume 180 (2022) 113185, ISSN 0920-3796, https://doi.org/10.1016/j.fusengdes.2022.113185.

[35] G. Demeneghi, B. Barnes, P. Gradl, D. Ellis, J. R. Mayeur, K. Hazeli, Directed energy deposition GRCop-42 copper alloy: Characterization and size effects, Materials & Design, Volume 222 (2022) 111035, ISSN 0264-1275, https://doi.org/10.1016/j.matdes.2022.111035.

[36] P. Gradl, O. R. Mireles, C. Katsarelis, T. M. Smith, J. Sowards, A. Park, P. Chen, D. C. Tinker, C. Protz, T. Teasley, D. L. Ellis, C. Kantzos, Advancement of extreme environment additively manufactured alloys for next generation space propulsion applications, Acta Astronautica, Volume 211 (2023) Pages 483-497, ISSN 0094-5765, https://doi.org/10.1016/j.actaastro.2023.06.035.

[37] Tata, B.V.R., Raj, B. Confocal laser scanning microscopy: Applications in material science and technology. Bull Mater Sci 21, 263–278 (1998). https://doi.org/10.1007/BF02744951

[38] S. Ghosh, J. Choi, Three-dimensional transient finite element analysis for residual stresses in the laser aided direct metal/material deposition process, J. Laser Appl. 17 (2005) 144–158.

[39] P. Mercelis, J.P. Kruth, Residual stresses in selective laser sintering and selective laser melting, Rapid Prototyp. J. 12 (2006) 254–265.

[40] L. Wang, S.D. Felicelli, P. Pratt, Residual stresses in LENS-deposited AISI 410 stainless steel plates, Mater. Sci. Eng. A 496 (2008) 234–241.

[41] E. Punzel, F. Hugger, R. Dörringer, T. L. Dinkelbach, A. Bürger, Comparison of different system technologies for continuous-wave laser beam welding of copper, Procedia CIRP, Volume 94 (2020) Pages 587-591, ISSN 2212-8271, https://doi.org/10.1016/j.procir.2020.09.081.

Appendix I: Longitudinal Residual Strain data in Top (8^{th}), Middle (4^{th}) and Bottom (1^{st}) layers of the 8-layer sample measured from EDD. The residual strain value is calculated from the averaged intensity data through 21 diffraction angles

Position in x direction	Layer 8	Layer 4	Layer 1
1.08016	0.001795	0.001145	0.001639
1.16002	0.001999	0.001759	0.002119
1.24018	0.001763	0.001713	0.001866
1.32004	0.001298	0.001745	0.002451
1.08016	0.001432	0.002596	0.002295
1.48006	0.001802	0.002772	0.00216
1.56022	0.001979	0.003153	0.000692
1.64008	0.001247	0.001384	0.00146
2.23997	0.000888	0.002172	0.001959
3.84021	0.001325	0.001726	0.001257
5.44011	0.001363	0.001902	0.001778
7.04001	0.002069	0.001892	0.001468
8.64021	0.002064	0.001359	0.001535
10.24001	0.001478	0.001446	0.001562
11.84021	0.00163	0.001786	0.001703
13.42001	0.001623	0.001908	0.001525
13.50021	0.001374	0.00138	0.001571
13.58001	0.001415	0.00226	0.001745
13.66021	0.001038	0.00234	0.001682

13.74011	0.000974	0.001354	0.001727
13.82021	0.001277	0.001061	0.001628
13.90011	0.001192	0.00159	0.001401
13.98021	0.00042	0.001204	0.001504

Appendix II: Normalized Square Root Mean Error of Different Peak Fitting Method for Peak [3,1,1] in Scan #20

Single Strain	Robust	Least Square
4.89%	3.51%	3.44%